Geoscience Letters

RESEARCH LETTER

Open Access

Modeling the 2024 Noto Peninsula earthquake tsunami: implications for tsunami sources in the eastern margin of the Japan Sea

Hidetoshi Masuda[1], Daisuke Sugawara[2*], An-Chi Cheng[3], Anawat Suppasri[2], Yoshinori Shigihara[4], Shuichi Kure[5] and Fumihiko Imamura[2]

Abstract

A moment magnitude (M_w) 7.5 earthquake occurred on January 1, 2024, at the northern tip of the Noto Peninsula, Central Japan, triggering a large tsunami. Seismological and geodetic observations revealed the rupture of mapped submarine active faults. While proximal segment ruptures have been well resolved by previous research, far offshore segments have posed challenges for onshore-based inversions. This emphasizes the necessity for a comprehensive study on the fault through tsunami modeling. Here, we aimed to examine tsunami propagation and inundation using four different fault models to identify the general characteristics of the tsunami source and evaluate the complexities of earthquake- and submarine landslide-induced tsunamis. We identified the simultaneous rupture of two active fault systems as the most suitable model for explaining observed tsunami height and inundation; however, some inconsistencies with observations remained. The propagation process did not follow a concentric pattern but aligned with bathymetric heterogeneity. The findings also suggested potential amplification effects responsible for the devastation of the coast of Iida Bay and indicated a possible submarine landslide in southern Toyama Bay. The findings of the present work could benefit the exploration of a more realistic tsunami source model, considering the differences between observations and simulations. Such efforts, in collaboration with paleotsunami research, can contribute to the improved assessment of hazards from submarine active faults.

Keywords Eastern margin of the Japan Sea, Submarine active fault, Submarine landslide, Paleotsunami

Introduction

On January 1, 2024, a magnitude (M_w) 7.5 earthquake occurred at a depth of 15.5 km north of the Noto Peninsula, Japan (U. S. Geological Survey 2024). Immediate tsunami warnings were issued, and tsunami waves were observed along the coasts of the Japan Sea, including South Korea, and Russia (Intergovernmental Oceanographic Commission [IOC] 2024). In Japan, the tsunami caused damage to coastal areas on the eastern coast of the Japan Sea, such as Ishikawa, Toyama, and Niigata Prefectures.

Government-commissioned projects were undertaken in the region to assess earthquake and tsunami hazards. The Ministry of Land, Infrastructure, Transport, and Tourism (MLIT) organized the Research and

*Correspondence:
Daisuke Sugawara
daisuke.sugawara.b3@tohoku.ac.jp
[1] Department of Earth Science, Graduate School of Science, Tohoku University, 6-3 Aramaki Aza Aoba, Sendai, Miyagi 980-8578, Japan
[2] International Research Institute of Disaster Science, Tohoku University, 468-1 Aramaki Aza Aoba, Sendai, Miyagi 980-8572, Japan
[3] Civil and Environmental Engineering, Graduate School of Engineering, Tohoku University, 6-6-06 Aramaki Aza Aoba, Sendai, Miyagi 980-8579, Japan
[4] Department of Civil and Environmental Engineering, National Defense Academy, 1-10-20 Hashirimizu, Yokosuka, Kanagawa 239-8686, Japan
[5] Department of Environmental and Civil Engineering, Faculty of Engineering, Toyama Prefectural University, 5180 Kurokawa, Imizu, Toyama 939-0398, Japan

Examination Meeting on the Large-Scale Earthquake in the Japan Sea, a decade before the earthquake, to develop hypothetical fault models for tsunami hazard assessments on the Japan Sea Coast (MLIT 2014). Subsequently, the Ministry of Education, Culture, Sports, Science, and Technology organized the Integrated Research Project of Earthquake and Tsunami in the Sea of Japan, focusing on investigating active submarine faults in the Japan Sea. These projects had already mapped an active fault that potentially ruptured on January 1, 2024.

Seismic and geodetic observations indicate the presence of seismo- and tsunamigenic faults extending east offshore of the northern Noto Peninsula (Geospatial Information Authority of Japan [GSI] 2024a). Understanding the mechanisms underlying offshore submarine faulting is crucial for interpreting the tsunamis' waveforms, propagation, and inundation processes. In this study, we conducted numerical modeling of the 2024 Noto Peninsula earthquake tsunami, utilizing previously published hypothetical fault models and global navigation satellite system (GNSS)- and synthetic aperture radar (SAR)-based preliminary fault models (GSI 2024a) of the earthquake. We examined tsunami propagation and inundation processes by comparing simulations with available observations to depict the general characteristics of the tsunami source. In addition, we explored the potential contribution of submarine landslides to elucidate the recorded tsunami events further.

Data and methods

Tsunami observations

To understand the tsunami waveform features and behavior of the Noto Peninsula earthquake tsunami, we collected and processed sea-level records from eight tide gauge stations along the Japan Sea Coast. The IOC provides sea-level records from Toyama, Sado, Fukaura, and Saigo (http://www.ioc-sealevelmonitoring.org/news.php). In addition, the GSI published digital wave signals from the Kashiwazaki, Mikuni, Oga, and Tobishima tide gauge stations (https://www.gsi.go.jp/kanshi/tide_furnish.html). The sea-level record data provided by the IOC and GSI include ocean tides with sampling durations of 1 min and 30 s, respectively. To obtain tsunami signals, we applied a high-pass filter with a cutoff frequency of 0.000069444 Hz (14,400 s) to filter out the ocean tide from the original sea-level records. This filtering approach has been employed in previous studies to extract tsunami signals (Cheng et al. 2023a, b; Heidarzadeh and Satake 2013; Wang et al. 2022). For the analysis, we selected sea-level records from 06:00:00 UTC until 16:00:00 UTC on January 02, 2024, encompassing the period surrounding the January 2024 Noto earthquake at 07:10:09 (UTC). The observed tsunami waveforms served as references for the validation of the numerical tsunami simulation. The observed tsunami waveforms and locations of the tide gauge stations are shown in Fig. 1.

The tsunami event was monitored at eight tide gauge stations along the Japan Sea Coast (Fig. 1). Following the M_w 7.5 earthquake, the initial wave was recorded at Sado station at 7:35 UTC, with an amplitude of 10.9 cm, and at Kashiwazaki station at 7:36 UTC, with an amplitude of 40.2 cm. Subsequent arrivals were observed at Tobishima (amplitude: 15.8 cm, time: 7:59 UTC), Oga (amplitude: 7.9 cm, time: 8:02 UTC), Fukaura (amplitude: 7.1 cm, time: 8:07 UTC), Mikuni (amplitude: 10 cm, time: 08:07 UTC), and Saigo (amplitude: 6.8 cm, time: 08:30 UTC) stations. All stations, except Toyama station, registered the first wave with a positive phase. Toyama station, situated approximately 50 km from the earthquake epicenter within Toyama Bay, experienced the initial tsunami wave at 7:15 UTC, about 5 min post-earthquake, displaying a distinct negative amplitude of −47.2 cm, suggesting a potential additional tsunami source within the bay. "Possible landslide-induced tsunami" offers a comprehensive analysis of the potential landslide source in Toyama Bay and its influence on the recorded tsunami signals at Toyama station.

The maximum crest waves varied from 27.1 cm (Saigo station) to 79.4 cm (Toyama station). Notably, Kashiwazaki station recorded the largest initial crest, whereas the maximum crest occurred later at the other stations. Across these seven stations, the maximum wave was observed between 10 min (Toyama station) and 140 min (Mikuni station) after the first arrival at the tide gauge stations. Persistent oscillations in the subsequent phases were observed at all stations. These amplified tsunami waves and prolonged durations at tide gauge stations can be attributed to reflections and the presence of trapped edge waves, along with the excitation of bay oscillations due to the shallow bathymetry and unique geomorphology along the Japan Sea Coast (Namegaya and Satake 2008). Detailed information and physical characteristics of the observed tsunami waveforms at each tide gauge station are summarized in Table 1.

Previous research has highlighted discrepancies between raw data from well (float)-type tide gauges and the "actual" waveform on the sea (e.g., Noye 1974; Namegaya et al. 2009). Owing to the connection of the well to the sea via long and/or narrow intake pipes, short- or intermediate-period signals, including tsunamis, are not fully reflected in the water height within the well. Consequently, adjustments accounting for the tide gauge response are necessary to accurately estimate the true tsunami waveform. Namegaya et al. (2009) conducted in situ experiments to determine site-specific coefficients for the correction formula

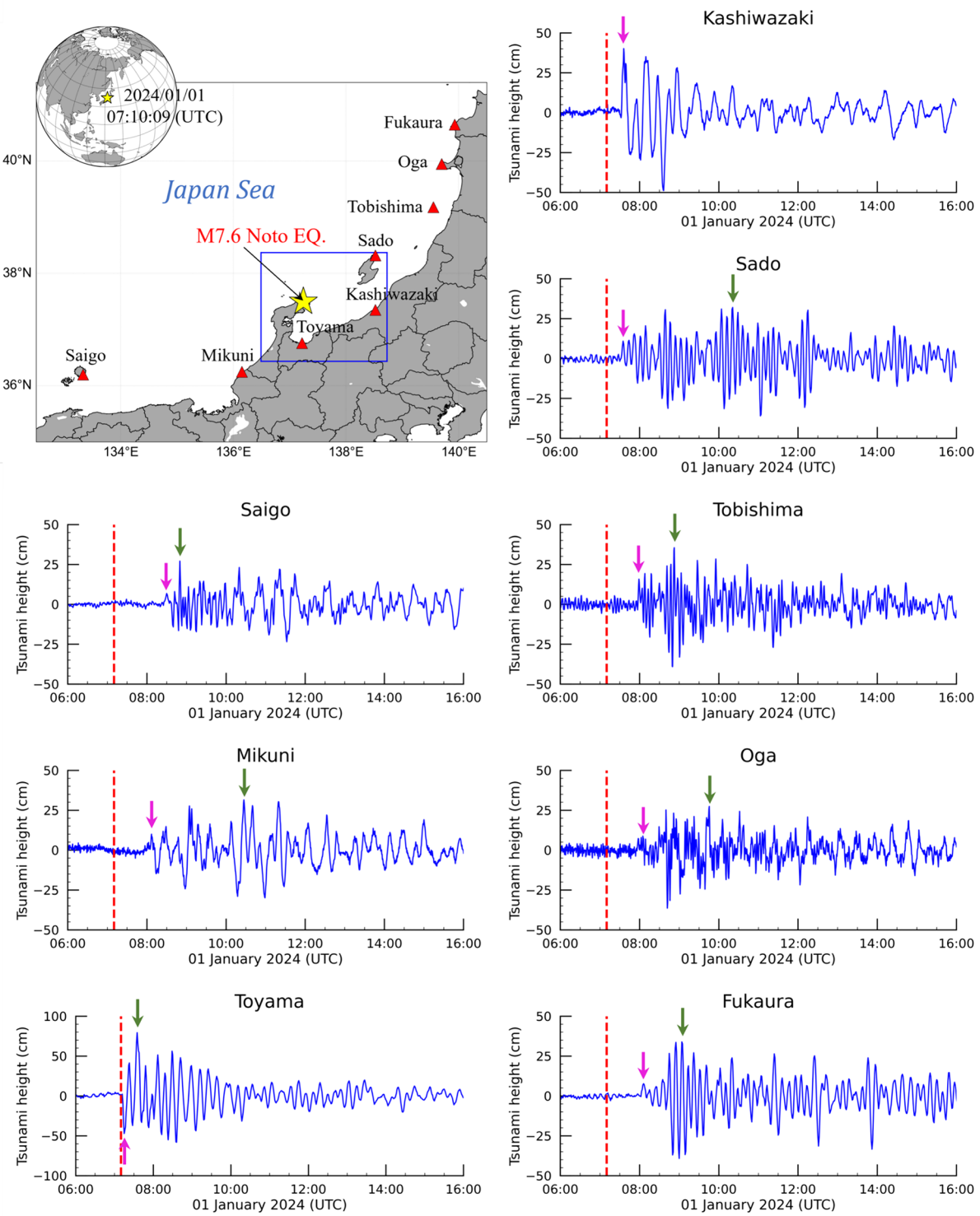

Fig. 1 Locations of the tide gauge stations and observed tsunami waveforms of the 2024 Noto earthquake. The epicenter is indicated using a yellow star. The tide gauge stations are plotted using red triangles. The dashed red lines indicate the earthquake occurrence times (EOTs). The magenta and green arrows denote the arrival times of the first wave and maximum crests, respectively

Table 1 Observed tsunami waveform features at tide gauge stations following the 2024 Noto Peninsula earthquake

Station	Type	Longitude (°E)	Latitude (°N)	Tsunami wave amplitude (cm)		Tsunami arrival time (UTC)	
				First wave	Maximum crest	First wave	Maximum crest wave
Saigo	Radar	133.33	36.2	6.8	27.1	8:30	8:50
Mikuni	Well	136.15	36.25	10	31.5	8:07	10:27
Toyama	Radar	137.22	36.76	−47.2	79.4	7:15	7:35
Kashiwazaki	Well	138.52	37.35	40.2	40.2	7:36	7:36
Sado	Radar	138.52	38.32	10.9	32	7:35	10:21
Tobishima	Well	139.55	39.18	15.8	35.5	7:59	8:52
Oga	Well	139.7	39.95	7.9	27.4	8:02	9:45
Fukaura	Radar	139.93	40.65	7.1	33.9	8:07	9:04

The amplitudes were calculated relative to the sea level at the time of the main shock, M_w 7.5, at 07:10:09 UTC

proposed by Noye (1974). These coefficients were established at Kashiwazaki station (also known as Kujiranami station in Namegaya et al. 2009) during experiments in September 2007. Assuming no changes in the pipe conditions since their measurements, we applied their formula and coefficients to correct the tsunami records at Kashiwazaki station. While Mikuni, Oga, and Tobishima stations are also of the well-type, their records remained uncorrected owing to the unavailability of site-specific coefficients. Following the correction procedure described by Namegaya et al. (2009), the maximum tsunami height at Kashiwazaki station nearly tripled to 1.13 m (Fig. 2c). The initial observed wave was separated into several short-period waves, and the later phase of the waves exhibited a shift to an earlier time.

Seismic tsunami source models

Four fault models (Cases #1–4) were tested to compare tsunami waveforms and inundation areas (Tables 2 and S1). In Case #1, fault model F43 (M_w 7.57) comprised two southeastward-dipping reverse faults (MLIT 2014), with their locations and dimensions determined from seafloor observations (Inoue and Okamura 2010). Although not directly related to the 2024 earthquake, F43 exhibited similarities, such as proximity to the mainshock hypocenter and dimensions resembling aftershock distributions. Despite a discrepancy in coseismic uplift (F43: ~2.5 m; field observations: >4 m; Ishiyama et al. 2024), they were relatively close. The F43 model assumed a slip amount of 4.5 m, which is 1.5 m larger than the scaling law value (Irikura and Miyake 2001).

The aftershock distribution extended further east of fault F43, coinciding with the F42 fault system. Therefore, the simultaneous ruptures of the F42 and F43 faults were examined (Case #2; M_w 7.66). We also examined another simultaneous rupture of the F43 and western subfault of F42 (hereafter F42w) (Case #3; M_w 7.60). The fault parameters for F42, as provided by MLIT (2014), indicate northwest-dipping reverse faults. The independent rupture of F42 was ruled out because the observed strong motion and coseismic uplift required a rupture beneath the northern Noto Peninsula. Case #4 (M_w 7.48) comprises the preliminary fault model for the 2024 Noto Peninsula earthquake by GSI, based on coseismic crustal deformation at GNSS-based control stations and SAR observations (GSI 2024a; as of February 29, 2024). The GSI fault model is composed of these subfaults to reproduce large and heterogeneous coseismic crustal deformation. The tsunami source (initial sea-surface displacement) was assumed to be identical to the vertical seafloor displacement calculated using Okada's (1985) formula. The rise time for the rupture was set to 30 s to mitigate the numerical oscillation caused by the large dislocation of the initial sea level.

Tsunami numerical simulation

The nonlinear shallow-water numerical model, TUNAMI-N2, was used to examine tsunami propagation and inundation (Goto et al. 1997). Bottom friction energy loss was considered by applying Manning's law, assuming a roughness coefficient of 0.025 $m^{-1/3}$ s. The governing equation was discretized using the leap-frog scheme on a nested staggered grid system with varying spatial resolutions (dx) of 135, 45, 15, and 5 m to reproduce tsunami propagation in the open ocean and the inundation of coastal areas (Fig. S1).

To maintain the computational stability, we selected temporal grid size of 0.05 s. The initial tide level was set to 0.15 m to approximate the general tide level during the earthquake. Bathymetric and topographic data were sourced from MLIT (2014) to generate the coarsest grid (dx = 135 m). Other grids with finer resolutions (dx = 45, 15, and 5 m) were developed using the digital

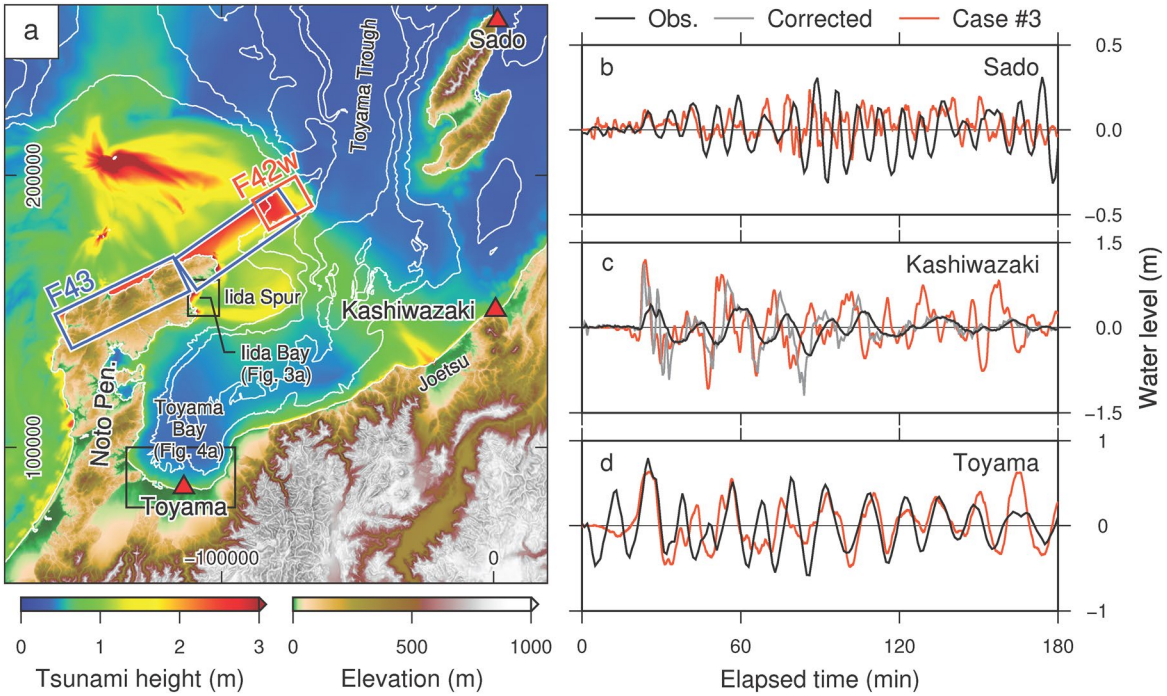

Fig. 2 Simulated regional tsunami height and time history of the water levels at selected tide stations for Case #3 (F42w and F43 fault models). **a** Maximum tsunami height with locations of the F42w and F43 fault models. Annotations along the vertical and horizontal axes in **a** indicate the northing and easting (unit: m) from the reference point (36° 0′ N, 138° 30′ E), respectively. White lines indicate isobaths with 500 m intervals. **b**–**d** Comparison of the time series of the observed and computed water levels at three tide stations (**b**: Sado, **c**: Kashiwazaki, **d**: Toyama). The corrected waveform at the Kashiwazaki station was processed following Namegaya et al. (2009)

bathymetric chart (M7011 Sado) published by the Japan Hydrographic Association and the digital elevation model (50 and 5 m grids) provided by the GSI.

Results

Comparison of observed and simulated tsunami waveforms

The simulated tsunami waveforms spanning 3 h at the Sado, Kashiwazaki, and Toyama tide stations were compared with the processed tsunami records. Among the four scenarios tested, Case #3 (simultaneous rupture of F42w and F43) provided the best explanation for the observations (Fig. 2b–d).

At Sado station, the observed waveform exhibited amplification approximately 90 min after the earthquake (Fig. 2b). Similarly, the computed waveform of Case #3 also showed amplification approximately 90 min after the earthquake, with a maximum height of 23.3 cm. Although the maximum amplitude was slightly lower than that observed, the later phase of the simulated

Table 2 Earthquake fault parameters (MLIT 2014; GSI 2024a)

Fault model	Longitude (°E)	Latitude (°N)	Top end depth (km)	Length (km)	Width (km)	Strike (°)	Dip (°)	Rake (°)	Slip (m)	M_w[a]
F43	136.6811	37.3274	1.0	48.3	19.7	64	45	113	4.5	7.57
	137.1753	37.5179	1.0	45.9	19.7	55	45	105	4.5	
F42	137.8939	38.0095	1.0	37.7	17.7	201	45	78	3.1	7.28
	137.7436[b]	37.6983[b]	1.0	18.1	17.7	241	45	112	3.1	
GSI (2024a)	136.68	37.246	0.1	22	12.2	22.7	40.6	84.4	6.79	7.48
	136.876	37.414	0.0	16.2	20.4	78.3	54.9	140.2	2.83	
	137.037	37.445	0.1	66.8	11.5	53.3	49.7	114.6	4.42	

[a] Assuming rigidity of 34 GPa (MLIT 2014)

[b] Referred to as F42w

waveform resembled a spindle shape, akin to the observation. This characteristic later phase was induced by an edge wave propagating along the northern shore of the island (Movie S1). Following the initial amplification, the simulated tsunami gradually attenuated, with a second amplification observed approximately 3 h after the earthquake. Cases #1 and #4 resulted in considerably lower tsunami heights than those observed (Figs. S2 and S4). Notably, the computed first tsunami arrival time (Case #2) was faster than that observed by approximately 5 min (Fig. S3), while the maximum tsunami height was closer to the observation than in Case #3. Given the significance of tsunami arrival time over later amplitude, we focused on Case #3 rather than #2.

At Kashiwazaki station, simulated water levels from all fault models tended to overestimate the amplitude of the raw data (Figs. 2c, S2c, S3c, and S4c). However, the simulations showed better consistency with the corrected waveform. The maximum tsunami height for Case #3 was 1.19 m, which closely matched the corrected maximum (1.13 m). In addition, the tsunami arrival time and wave period of the first wave in Case #3 closely aligned with the corrected data.

The observed and computed waveforms for Case #3 exhibited good agreement at Toyama station (Fig. 2d). Apart from the first wave, both the simulated amplitude and wave period closely matched the observation. The maximum amplitude observed was 79.4 cm, whereas the simulation recorded 63.2 cm. Notably, the arrival time of all simulated first waves matched the timing of the observed second wave (Figs. 2d, S2d, S3d, and S4d). This discrepancy suggests that the seismic tsunami source along and offshore of the northern coast of the Noto Peninsula alone cannot fully explain the observations, implying the presence of an additional tsunami source near Toyama station.

Simulated regional tsunami heights

The simultaneous rupture of the F43 and F42w faults caused considerable convergence of the tsunami in the northern offshore region of the Noto Peninsula and Joetsu Coast (Fig. 2). The rupture of F43, combined with wave refraction due to bathymetry, remarkably amplified the tsunami in the northern offshore of the Noto Peninsula. A comparison with the single rupture of F43 (Case #1; Fig. S2) suggested that the additional rupture of F42w can explain the tsunami convergence and amplification on the southern Sado and Joetsu Coasts. The Japan Meteorological Agency (JMA) reported a large tsunami runup of 5.8 m at Joetsu and a trace height of 3.8 m at the southern Sado Island (JMA 2024). While direct comparison is hindered by the absence of exact coordinates and the coarse spatial resolution (dx = 135 m for regional tsunami propagation) of the simulations, these measurements serve as valuable tools for validating the simulations. We derived simulated tsunami heights at plausible locations based on the place names provided by JMA (2024). In Case #2, simulated tsunami heights near the runup locations closely approximated the observations, yielding 3.0 m at the southern Sado Island and 5.3 m at Joetsu. The subsequent closest simulation was Case #3, which resulted in tsunami heights of 1.7 and 4.1 m at the southern Sado Island and Joetsu, respectively. Conversely, Case #1 and #4 produced considerably lower tsunami heights (#1: 1.6 m at Sado, 2.0 m at Joetsu; #4: 1.2 m at Sado, 2.3 m at Joetsu), suggesting that these scenarios may not adequately explain the field measurements.

Tsunami propagation was considerably affected by the complex bathymetry (Movie S1). The eastern offshore area of the Noto Peninsula is characterized by a large water depth (Toyama Trough; > 1500 m depth), resulting in an earlier tsunami arrival on Sado Island (~ 10 min) than that on the eastern coast of the Noto Peninsula. Despite its proximity to the source, a tsunami of > 1 m arrived approximately ~ 20 min later at Iida Bay, an open bay located on the northeastern coast of the Noto Peninsula, owing to shallow bathymetry around the offshore Iida Spur. The wave amplification can be explained by refraction due to the bathymetry. One hour after the earthquake, a tsunami wave that converged in the northern offshore region of the Noto Peninsula refracted and propagated along the western coast of the peninsula. Notably, this later tsunami wave surpassed the height of the first wave at some locations.

Inundation process in the Iida Bay Coast

A post-tsunami airborne survey indicated that the coastal lowlands along Iida Bay were inundated extensively, with a maximum runup distance of approximately 400 m from the coastline (Geospatial Information Authority of Japan (GSI) 2024). The simulated tsunami inundations were compared with the mapped inundation areas published by GSI (2024b).

Among the four cases, Cases #2 and #3 provided the most comprehensive explanation for the overall inundation area (Figs. 3 and S6). Notably, the inundation at the Iida Port was only reproduced in these scenarios. Here, we focused on the result of Case #3, considering the above-mentioned consistencies with the waveform records. Since the general characteristics of tsunami propagation were similar among the scenarios, the differences in inundation were attributed to variations in wave heights.

The inundation primarily resulted from a second wave occurring 30–40 min after the earthquake in all computational scenarios (Figs. 3, S5, S6, and S7). The first wave

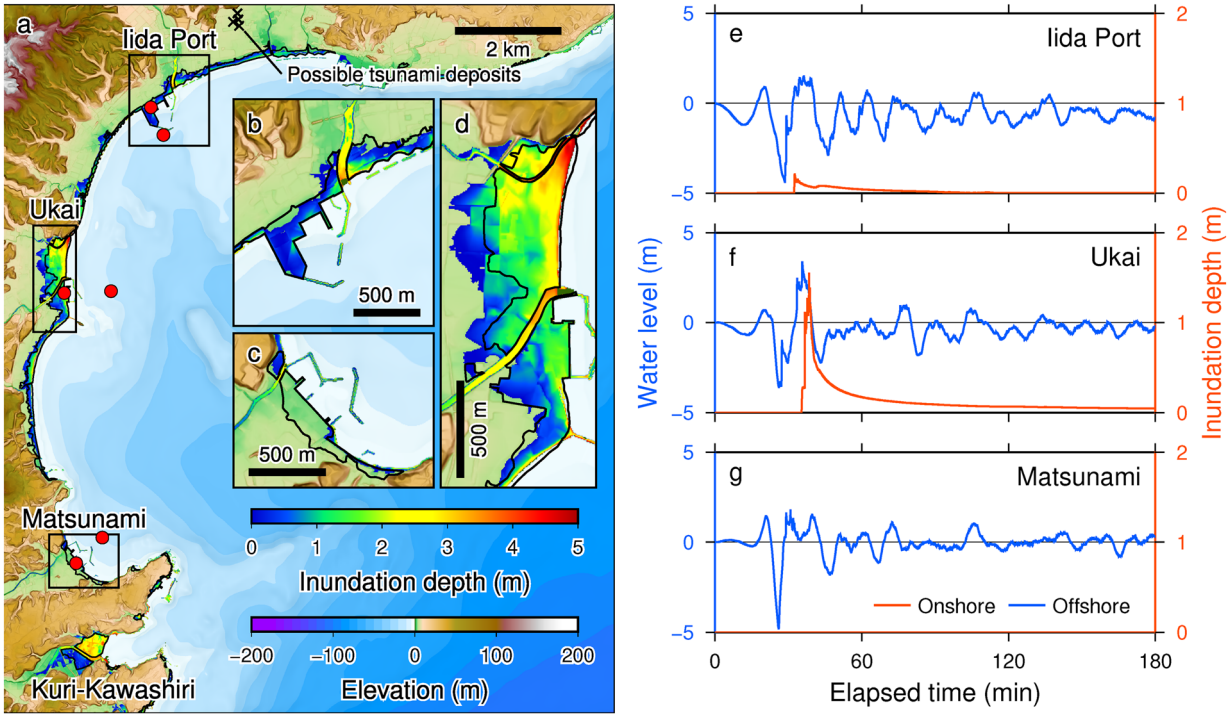

Fig. 3 Simulated tsunami inundation of the Iida Bay Coast and time history of the water levels for Case #3 (F42w and F43 fault models). **a** Distribution of the simulated inundation depth. Black solid line indicates the inundation area estimated from the aerial photo (GSI 2024b). Red circles represent the locations of virtual tsunami stations. Locations of possible tsunami deposits shown in black crosses are based on Urabe et al. (2015). **b**–**d** Enlarged view of the inundation depths in three selected areas (Iida Port, Ukai, and Matsunami). **e**–**g** Time series of the water levels at offshore (blue line) and inundation depths at onshore (red line) stations

did not contribute to the inundation in the Iida, Ukai, or Matsunami areas. The second wave propagated along the shore from south to north (Movie S2). In Case #3, the tsunami propagated from the north, causing inundation at Iida Port. Waves from the south and north were superimposed in front of the Ukai area, resulting in substantial amplification approximately 35 min after the earthquake, explaining the extensive inundation of the Ukai area.

Discussion

Implications for the active fault tsunami source

Comparing tsunami waveforms and inundation supported the scenario involving simultaneous ruptures of F42w and F43 (Case #3). This model also reproduces the high tsunami height on the coasts of Joetsu and southern Sado. In general, the GSI model (Case #4) generated the smallest tsunami among the four scenarios, underestimating both maximum amplitude and inundation substantially. While F43 (Case #1) caused a tsunami larger than that caused by the GSI model, the maximum amplitude at the Sado and Toyama stations and the inundation of Iida Port were underestimated. In contrast, the maximum amplitude and inundation were successfully reproduced in Case #2; however, the tsunami arrival at the Sado station was considerably faster than that of the observation.

Case #3 utilized tsunami sources constructed by MLIT (2014) designed for tsunami hazard assessments, which typically employ a larger magnitude to avoid underestimation. Assuming a crust rigidity at 34 GPa, the moment magnitude in Case #3 was calculated as M_w 7.60, exceeding the instrumental observation of M_w 7.5. Better tsunami rupture models that explain not only the observed tsunami waveforms and inundation but also the geodetic and seismic observations should be explored in future works. Estimating a sophisticated tsunami source model requires quantitative comparisons of tsunamis and other geophysical data with simulations; however, this is beyond the scope of the current study. However, we attempted to obtain the general characteristics of the tsunami source based on our simulations.

The notable disparity between the simulated and raw waveforms at Kashiwazaki station is notably rectified through data correction, taking into account the tide gauge response (Fig. 2c; e.g., Namegaya et al. 2009). This underscores the critical importance of waveform correction at well-type tide stations in tsunami research.

Despite the extensive deployment of well-type stations along the northern Japan Sea Coast, the ramifications of well response and the necessity for data correction seem to have been overlooked (e.g., Fujii and Satake 2024). In addition to rectifying tsunami records from wells, tsunami hydrodynamic simulations may necessitate the utilization of high-resolution shallow bathymetric data and the inclusion of nonlinear terms (e.g., advection and bottom friction) to accurately capture tsunami waveforms at nearshore tide stations.

Following a thorough comparison between simulations and observations, Case #3, involving the simultaneous rupture of F42w and F43 faults, emerges as the most plausible explanation for the recorded tsunami behavior. However, since this study presents the results of forward simulations, no attempt was made to optimize the slip on each subfault. Consequently, further investigation is warranted to ascertain whether F42w indeed ruptured; a larger slip on the eastern tip of F43 could produce sea-surface displacement indistinguishable from the F42w rupture in Case #3. While this could be addressed through tsunami waveform inversion, it lies beyond the scope of the current study.

Our simulations were validated using tsunami records east of the Noto Peninsula, potentially leaving the western portion of the source fault inadequately constrained. Given its proximity to the land, the western portion caused large uplift in coastal areas. Crustal deformation was captured not only by GNSS stations but also by SAR observations. Thus, such geodetic data are immensely valuable in estimating the fault model (e.g., GSI 2024a). A comprehensive understanding of fault kinematics will likely emerge through the integration of GNSS and SAR data alongside tsunami records in the future.

Possible landslide-induced tsunami

One of the most important discrepancies between the observations and simulations was the waveform at the Toyama tide station during the early period (0–20 min). The numerical simulations indicated a delayed arrival of the seismic triggered tsunami compared to the arrival of the observed first wave, implying the presence of an additional tsunami source near the Toyama station.

Southern Toyama Bay is characterized by complex coastal fan deltas developed at the mouths of several torrential rivers drained from the high mountains. The submerged portions of the delta form steep continental slopes prone to submarine landslides. Many previous submarine landslides have been identified by analyzing bathymetric charts (Moriki et al. 2017). Based on the findings of the Japan Coast Guard (JCG) from post-2024 earthquake differential bathymetric surveys, large submarine landslides were reported near the Toyama tide station (JCG 2024b; Fig. 4a). These landslides occurred on both the left and right slopes of the submarine canyon, descending to the bottom of the channel. Considering these observations, we investigated the tsunami excitation potential of the submarine landslides through numerical simulation (Case #5; Table S1). Note that another submarine landslide has been identified in the eastern offshore area of the Noto Peninsula (JCG 2024a), more than 100 km away from the Toyama station. However, owing to the considerable distance, this submarine landslide may not have contributed to the earlier observed wave at the Toyama station.

To estimate the initial tsunami waveform resulting from the submarine landslides, we employed the formula proposed by Watts et al. (2005) for slides. This method approximates the initial sea-surface displacement (at the characteristic time t_o) using a double Gaussian shape. The landslide parameters used for the simulation are shown in Table S2. The parameters used for the simulation, including the locations and sizes of the slides and bathymetric-related parameters, were roughly estimated based on JCG (2024b). Other parameters were adopted from Watts et al. (2005). The displacements caused by the submarine landslides on the left and right slopes were combined (Fig. 4a) and added to the initial condition of the tsunami simulation. The maximum depression of the sea surface was 49 cm, and the upward displacements due to the slide movement were completely offset by the depression.

Given that large ground acceleration, which promotes submarine landslides, might delay the earthquake occurrence time (EOT) since the location of the submarine landslide is approximately 80 km away from the focal region, we considered the observation of ground motion at the TYMH03 station (Fig. 4a; KiK-net installed by the National Research Institute for Earth Science and Disaster Resilience). The peak ground acceleration appeared around 50 s after EOT, and t_o was calculated as 39.6 s (Grilli and Watts 2005). Consequently, we instantaneously imposed the landslide-induced initial sea-surface displacement on the simulated water level at 89.6 s after EOT. Note that the seismic tsunami source of Case #5 was identical to that of Case #3 (Table S1).

As depicted in Fig. 4b, the simulation including the submarine landslide tsunami source reproduced the arrival time of the first negative wave. However, the differences between water levels with and without the submarine landslide rapidly diminished, suggesting that the early tsunami arrival at the Toyama tide station was caused by the submarine landslides in front of the station, and the landslide's effect attenuated quickly. Although the simulated amplitude and wave period of the first negative wave did not align with the observation,

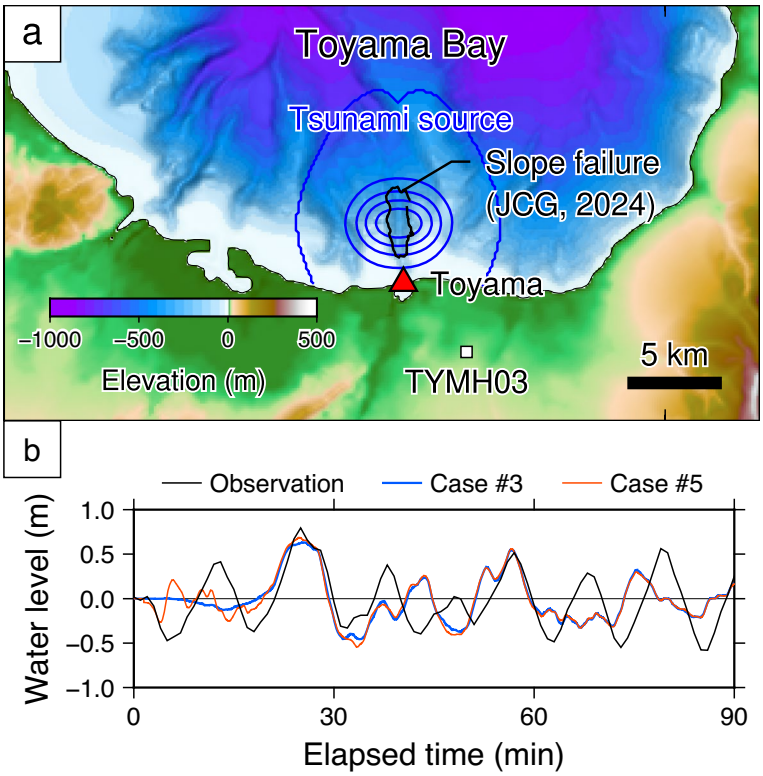

Fig. 4 Location of submarine landslide tsunami source and comparison of the time series of the water levels at the Toyama tide station. **a** Location of the submarine landslide (JCG 2024b) and estimated tsunami source (depression). Contour interval for tsunami source is 10 cm. **b** Observed and simulated (Cases #3 and #5) time series of the water levels at the Toyama tide station

these discrepancies might be attributed to the simplification of landslide kinematics and the selection of landslide parameters. Nevertheless, given the validity of our simulation to some extent, these discrepancies imply the possible existence of other submarine landslide(s) that generated a tsunami with a larger amplitude and longer period. This potential unknown submarine landslide(s) may be located slightly further from the known slides within Toyama Bay, as the arrival time of the first negative wave has already been explained by the presented simulation.

Relevant past events

The tsunami simulations showed that the inundation of Iida and Toyama Bays and the western coast of the Noto Peninsula was predominantly caused by the eastern segment of F43 and probably F42w (Fig. 2a and Movie S1). This region has been evaluated for tsunami hazards from active submarine faults based on paleoseismological studies both onshore and offshore (e.g., Inoue and Okamura 2010; Shishikura et al. 2020; Takashimizu et al. 2020).

In 2007, an M_j 6.9 earthquake occurred on an active fault in the north-western offshore region of the Noto Peninsula (Monzen-oki segment; Inoue and Okamura 2010). Bathymetric surveys have identified other shore-parallel offshore active faults on the northern coast of the peninsula (Inoue and Okamura 2010). The 2024 earthquake could be explained by multi-segment ruptures of known offshore active faults. The F43 fault (Case #1), which was constructed by the governmental tsunami hazard assessment (MLIT 2014), mimicked the Saruyama-oki, Wajima-oki, and Suzu-oki segments, as reported by Inoue and Okamura (2010). Shishikura et al. (2020) identified three marine terraces (L1–L3) on the northern coast of the peninsula formed in the last 6000 years, suggesting past coseismic uplift; however, their formation ages are uncertain. Since the up-dip end of the fault is close to the present shoreline, a large coseismic uplift was observed after the 2024 event (Ishiyama et al. 2024; Shishikura et al. 2024). The post-event field survey reported that the coastal uplift formed a new terrace, "L4," due to the 2024 earthquake (Shishikura et al. 2024). Therefore, paleoseismological findings imply the past recurrence of earthquakes similar to the 2024 event. Although tectonic geomorphology has identified past activity in the proximal portion of the F43 fault, the seismicity of the distant segments, which caused tsunami inundations at many locations, is difficult

to understand from onshore records. Instead, tsunami deposits provide evidence of past tsunamigenic submarine faults (Takashimizu et al. 2020). Around the Noto Peninsula and Toyama Bay, earlier geological investigations have discovered tsunami deposits (Takashimizu et al. 2020 and references therein). In the coastal lowlands of Iida Bay, Urabe et al. (2015) found two layers of possible tsunami deposits dated to approximately 2500 and 3500 years ago. The possible paleotsunami deposits are distributed far beyond the inundation limit of the 2024 tsunami (Fig. 3a). The paleoseismological findings should be reviewed by analyzing the 2024 earthquake to reveal the relationship between the latest event and the causal events of the possible tsunami deposits. Paleotsunami records in the eastern margin of the Japan Sea are sparse compared to those on the Pacific Coast of Japan (Takashimizu et al. 2020). Insights into the timing and magnitude of historical tsunamis, obtained through geological studies, are pivotal for enhancing our understanding of past rupture patterns of the active faults. These findings can be further elucidated through numerical modeling of paleotsunami sources.

Submarine landslides in Toyama Bay could explain the tsunami arrival time at the Toyama station (Fig. 4b). A similar submarine landslide and subsequent tsunami were reported in Toyama Bay during the 2007 Noto earthquake (Abe et al. 2008). Previous investigations of bathymetric features clarified the distribution of past submarine landslides within the bay (Moriki et al. 2017). While dozens of submarine landslides have been documented in Toyama Bay, there have been no prior reports of landslides occurring directly in front of the Toyama tide station (Abe et al. 2008; Moriki et al. 2017). Therefore, a sufficient amount of sediment, ready to slide, may have accumulated at these locations, highlighting the importance of mapping past submarine landslides and slope susceptibility to ground motions in tsunami hazard assessments.

Conclusions

Offshore active faults along the eastern margin of the Japan Sea have been extensively studied in recent years, both through governmental projects and by individual researchers across various disciplines (e.g., Takashimizu et al. 2020). Tectonic geomorphology investigations on uplifted marine terraces along the northern Noto Peninsula suggest that the 2004 earthquake was a rare event occurring once every several thousand years (Shishikura et al. 2020). While predicting the timing or assessing the annual probability of occurrence of a large earthquake on intraplate active faults remains challenging, a comparison of tsunami simulations with observed records indicates that the anticipated mechanism, extent, and magnitude of the tsunamigenic earthquake were accurately predicted. In addition, probabilistic hazard assessment has underscored the high probability of large tsunamis in the study area (Mulia et al. 2020), highlighting the importance of multidisciplinary research into offshore active faults, incorporating geomorphological, geophysical, and geological approaches.

The findings also shed light on the challenges in tsunami hazard assessment, particularly regarding the potential simultaneous rupture of multi-segment fault systems (i.e., F43 and F42w), as well as the presence of additional tsunami sources associated with submarine landslides, the probability of which is difficult to evaluate. Tsunami-related paleoseismology, such as research on tsunami deposits, could offer valuable insights into past catastrophic events caused by offshore active faults and submarine landslides. These insights could provide a more comprehensive understanding of seismic and tsunami hazards in the eastern margin of the Japan Sea.

Abbreviations

EOT	Earthquake occurrence time
GNSS	Global Navigation Satellite System
GSI	Geospatial Authority of Japan
IOC	Intergovernmental Oceanographic Commission
JCG	Japan Coast Guard
JMA	Japan Meteorological Agency
MLIT	Ministry of Land, Infrastructure, Transport and Tourism
SAR	Synthetic aperture radar

Supplementary Information

The online version contains supplementary material available at https://doi.org/10.1186/s40562-024-00344-8.

Supplementary Material 1: Fig. S1. Nesting grid system used for the numerical simulations. Rectangles indicate the outline of domains. The spatial resolutions of the domain are A: 135 m, B: 45 m, C: 15 m, and D: 5 m from outside to inside. Fig. S2. Simulated regional tsunami height and time history of water levels at selected tide stations for Case #1 (F43 fault model). (a) Maximum tsunami height with locations of the F43 fault. Annotations along the vertical and horizontal axes in panel (a) indicate the northing and easting (unit: m) from the reference point (36° 0′ N, 138° 30′ E), respectively. White lines indicate isobaths with 500 m intervals. (b–d) Comparison of the time series of the observed and computed water levels at three tide stations (b: Sado, c: Kashiwazaki, d: Toyama). Fig. S3. Simulated regional tsunami height and time history of water levels at selected tide stations for Case #2 (F42 and F43 fault models). Details are the same as those in Fig. S2. Fig. S4. Simulated regional tsunami height and time history of water levels at selected tide stations for Case #4 (GSI fault model). Details are the same as those in Fig. S2. Fig. S5. Simulated tsunami inundation of the Iida Bay Coast and time history of water levels for Case #1 (F43 fault model). (a) Distribution of the simulated inundation depth. The black solid line indicates the inundation area estimated from the aerial photo (GSI 2024b). Red circles represent the locations of the virtual tsunami stations. (b–d) Enlarged view of the inundation depths in three selected areas (Iida Port, Ukai, and Matsunami). (e–g) Time series of the water levels at offshore (blue line) and inundation depths at onshore (red line) stations. Fig. S6. Simulated tsunami inundation of the Iida Bay Coast and time history of water levels for Case #2 (F42 and F43 fault models). Details are the same as those in Fig. S5. Fig. S7. Simulated tsunami inundation of the Iida Bay Coast and time history of water levels for Case #4 (GSI fault model). Details are the same as those in Fig. S5. Table S1. List of model runs. Table S2. Parameters of the submarine landslide used in the simulation of Case #5.

Supplementary Material 2: Movie S1. Tsunami propagation process (Case #3) for 3 h after the earthquake. The initial tidal level was then determined.

Supplementary Material 3: Movie S2. Tsunami propagation and inundation processes (Case #3) 30–60 min after the earthquake.

Acknowledgements
The authors thank Masaki Iida at the Graduate School of Science, Tohoku University, for providing information on paleoseismological studies in the study area. Constructive comments received from two anonymous reviewers greatly improved the manuscript. We also thank Editage (www.editage.jp) for English language editing.

Author contributions
HM and DS performed the numerical simulations and analyzed the results. A-CC and AS processed and interpreted tidal records. YS collected information on submarine landslides in Toyama Bay. SK collaborated with the corresponding author during the discussion and writing of the manuscript. FI supervised the study. HM, DS, A-CC, and AS prepared the first draft of the manuscript. YS, SK, and FI revised the manuscript. All the authors have read and approved the current version of this manuscript.

Funding
This research was partially funded by JSPS KAKENHI (Grant Number 22H01606) and Pacific Consultants Co., Ltd. through the International Research Institute of Disaster Science (IRIDeS) at Tohoku University.

Availability of data and materials
The original tidal records are available at http://www.ioc-sealevelmonitoring.org/news.php (IOC) and https://www.gsi.go.jp/kanshi/tide_furnish.html (GSI). The mapped inundation area datasets are available at https://www.gsi.go.jp/BOUSAI/20240101_noto_earthquake.html#7 (GSI). Generic Mapping Tools software (Wessel et al. 2019; available at https://www.generic-mapping-tools.org/) was used for data handling and figure preparation. The other datasets used and/or analyzed in the current study are available from the corresponding author upon reasonable request.

Declarations

Competing interests
The authors declare that they have no competing interest.

Received: 9 February 2024 Accepted: 3 June 2024
Published online: 14 June 2024

References

Abe I, Goto K, Imamura F, Shimizu K (2008) Numerical simulation of the tsunami generated by the 2007 Noto Hanto Earthquake and implications for unusual tidal surges observed in Toyama Bay. Earth Planets Space 60:133–138. https://doi.org/10.1186/BF03352774

Cheng A-C, Suppasri A, Heidarzadeh M, Adriano B, Chua CT, Imamura F (2023a) Tsunami wave characteristics in Sendai Bay, Japan, following the 2016 Mw 6.9 Fukushima earthquake. Ocean Eng 287:115676. https://doi.org/10.1016/j.oceaneng.2023.115676

Cheng A-C, Suppasri A, Pakoksung K, Imamura F (2023b) Characteristics of consecutive tsunamis and resulting tsunami behaviors in southern Taiwan induced by the Hengchun earthquake doublet on 26 December 2006. Nat Hazards Earth Syst Sci 23:447–479. https://doi.org/10.5194/nhess-23-447-2023

Fujii Y, Satake K (2024) Slip distribution of the 2024 Noto Peninsula earthquake (M_{JMA} 7.6) estimated from tsunami waveforms and GNSS data. Earth Planets Space 76:44. https://doi.org/10.1186/s40623-024-01991-z

Geospatial Information Authority of Japan (GSI) (2024a) Preliminary earthquake fault model of the 2024 Noto Peninsula earthquake (as of February 29, 2024). https://www.gsi.go.jp/common/000253939.pdf. Accessed 2 Apr 2024. (**in Japanese, with English abstract**)

Geospatial Information Authority of Japan (GSI) (2024b) Inundation area of the 2024 Noto Peninsula earthquake tsunami inferred from aerial photographs. https://www.gsi.go.jp/BOUSAI/20240101_noto_earthquake.html#7. Accessed 18 Jan 2024. (**in Japanese, translated title**)

Goto C, Ogawa Y, Shuto N (1997) IUGG/IOC TIME project, numerical method of tsunami simulation with the leap-frog scheme. UNESCO, Paris, p 130

Grilli ST, Watts P (2005) Tsunami generation by submarine mass failure. I: modeling, experimental validation, and sensitivity analyses. J Waterw Port Coast Ocean Eng 131:283–297. https://doi.org/10.1061/(ASCE)0733-950X(2005)131:6(283)

Heidarzadeh M, Satake K (2013) Waveform and spectral analyses of the 2011 Japan tsunami records on tide gauge and DART stations across the Pacific Ocean. Pure Appl Geophys 170:1275–1293. https://doi.org/10.1007/s00024-012-0558-5

Inoue T, Okamura Y (2010) Explanatory notes of 1:200,000 marine geological map around the northern part of Noto Peninsula. Geological Survey of Japan, p 15. https://www.gsj.jp/data/coastal-geology/GSJ_DGM_S1_2010_01_b_sim.pdf. (**in Japanese, with English abstract**)

Intergovernmental Oceanographic Commission (IOC) (2024) Earthquake near West Coast of Honshu (Japan) https://www.ioc-sealevelmonitoring.org/news.php?p=show&id=9277. Accessed 5 Jan 2024

Irikura K, Miyake H (2001) Prediction of strong ground motions for scenario earthquake. J Geogr (chigaku Zasshi) 110:849–875. https://doi.org/10.5026/jgeography.110.6_849. (**in Japanese, with English abstract**)

Ishiyama T, Hirouchi D, Matta N, Tateishi R, Yasue K (2024) Coseismic coastal uplift associated with 2024 Noto Peninsula Earthquake (preliminary report 2). https://www.eri.u-tokyo.ac.jp/en/news/5994/. Accessed 18 Jan 2024

Japan Coast Guard (JCG) (2024a) Conformation of slope failure's trace in the sea bottom of eastern offshore of the Noto Peninsula. https://www.kaiho.mlit.go.jp/info/kouhou/r6/k240222/k240222.pdf. Accessed 9 Apr 2024. (**in Japanese, translated title**)

Japan Coast Guard (JCG) (2024b) Conformation of slope failure's trace in the sea bottom of Toyama Bay (second report). https://www.kaiho.mlit.go.jp/info/kouhou/r6/k240311_2/k240311_2.pdf. Accessed 3 Apr 2024. (**in Japanese, translated title**)

Japan Meteorological Agency (JMA) (2024) Report of the field survey of the 2024 Noto Peninsula earthquake tsunami by JMA-MOT. https://www.jma.go.jp/jma/press/2401/26a/20240126_tsunamichousakekka.pdf. Accessed 3 Apr 2024. (**in Japanese, translated title**)

Ministry of Land, Infrastructure, Transport and Tourism (MLIT) (2014) Final report of research and examination meeting on the large-scale earthquake in the Japan Sea. https://www.mlit.go.jp/river/shinngikai_blog/daikibojishinchousa/. Accessed 18 Jan 2024. (**in Japanese, translated title**)

Moriki H, Kumamoto T, Nakata T, Goto H, Izumi N, Nishizawa A (2017) Identification of landslide and its characteristics on the seafloor around Japan using anaglyph images. Rep Hydrogr Oceanogr Res 54:1–16 (**in Japanese, with English abstract**)

Mulia IE, Ishibe T, Satake K, Gusman AR, Murotani S (2020) Regional probabilistic tsunami hazard assessment associated with active faults along the eastern margin of the Sea of Japan. Earth Planets Space 72:123. https://doi.org/10.1186/s40623-020-01256-5

Namegaya Y, Satake K (2008) Tsunami generated by the 2007 Noto Hanto earthquake. Earth Planets Space 60:127–132. https://doi.org/10.1186/BF03352773

Namegaya Y, Tanioka Y, Abe K, Satake K, Hirata K, Okada M, Gusman AR (2009) In situ measurements of tide gauge response and corrections of tsunami waveforms from the Niigataken Chuetsu-oki earthquake in 2007. Pure Appl Geophys 166:97–116. https://doi.org/10.1007/s00024-008-0441-6

Noye BJ (1974) Tide-well systems III: improved interpretation of tide-well records. J Mar Res 32:183–194

Okada Y (1985) Surface deformation due to shear and tensile faults in a half-space. Bull Seismol Soc Am 75:1135–1154. https://doi.org/10.1785/BSSA0750041135

Shishikura M, Echigo T, Namegaya Y (2020) Activity of the off-shore active faults along the northern coast of the Noto Peninsula deduced from the height distribution of the lower marine terrace and emerged sessile

assemblage. Act Fault Res 53:33–49. https://doi.org/10.11462/afr.2020.53_33. (**in Japanese, with English abstract**)

Shishikura M, Namegaya Y, Echigo T (2024) Fourth report of the urgent investigation after the 2024 Noto Peninsula earthquake (coastal uplift). https://www.gsj.jp/hazards/earthquake/noto2024/noto2024-04.html. Accessed 18 Jan 2024. (**in Japanese, translated title**)

Takashimizu Y, Kawakami G, Urabe A (2020) Tsunamis caused by offshore active faults and their deposits. Earth-Sci Rev 211:103380. https://doi.org/10.1016/j.earscirev.2020.103380

U. S. Geological Survey (2024) M 7.5—2024 Noto Peninsula, Japan Earthquake. https://earthquake.usgs.gov/earthquakes/eventpage/us6000m0xl/executive, Accessed 22 Jan 2024

Urabe A, Yata T, Takashimizu Y, Kataoka K, Yamamoto H, Kamataki T, Sakai T, Sakai H, Takeuchi A, Hirakawa K (2015) Investigation of Tsunami deposits. In: Report of the integrated research project on seismic and tsunami hazards around the sea of Japan (FY2014), p 63–74. https://www.eri.u-tokyo.ac.jp/project/Japan_Sea/H26Report/PDF/11_H26JSPJ-C3.2.1.2.pdf. (**in Japanese, translated title**)

Wang Y, Heidarzadeh M, Satake K, Hu G (2022) Characteristics of two tsunamis generated by successive Mw 7.4 and Mw 8.1 earthquakes in the Kermadec Islands on 4 March 2021. Nat Hazards Earth Syst Sci 22:1073–1082. https://doi.org/10.5194/nhess-22-1073-2022

Watts P, Grilli ST, Tappin DR, Fryer GJ (2005) Tsunami generation by submarine mass failure. II: predictive equations and case studies. J Waterw Port Coastal Ocean Eng 131:298–310. https://doi.org/10.1061/(ASCE)0733-950X(2005)131:6(298)

Wessel P, Luis JF, Uieda L, Scharroo R, Wobbe F, Smith WHF, Tian D (2019) The generic mapping tools version 6. Geochem Geophys Geosyst 20:5556–5564. https://doi.org/10.1029/2019GC008515

Publisher's Note